FIELD MEASUREMENTS OF GPR ANTENNA PATTERN FOR AVA DATA CORRECTION

Aisha Abubakar KANA

Department of Geology and Mining, Nasarawa State University, Keffi, Nigeria

ABSTRACT: *Amplitude versus incidence angle (AVA) analysis is a multi – offset attribute analysis technique which involves relating amplitude variations with increasing angle of incidence (or practically, offsets), in order to characterize interfaces and layers. The GPR AVA technique has its origin from seismic reflection processing and assumes isotropic source radiation (and reception) for GPR and also, far – field conditions. GPR antennae radiate EM energy as waves travelling in a hemispherical wave front into the ground and, typically show a strong directionality in radiation and reception with respect to amplitude and/ or frequency of the signal when used for surface surveys. The antennae patterns depend on the properties of the media in which the GPR signal is radiated into and must, therefore be accounted for in AVA analysis. This paper reports the results of numerical simulations and field measurement of antennae patterns. The field site is Threshfield quarry, Yorkshire, United Kingdom, extracting the Carboniferous Limestone. A series of transillumination surveys, across limestone boulders of different thicknesses were done to enable in - situ determination of the antennae patterns. In addition to these and for comparison purposes, numerical simulations using GprMax software were also done. Both numerical and field data were processed using Reflex-Win Version 3.5.1 software (Sandmeier, 1997-2004). Processing comprises: de-wow (for field data), band – pass Butterworth filtering (250-750MHz), geometric spreading and envelope, or Hilbert transform. The resulting antennae patterns measured in the field agree broadly with numerically derived patterns, in that the basic shape is the same.*

KEYWORDS: GPR, Antennae Patterns, AVA

INTRODUCTION

Amplitude versus incidence angle (AVA) analysis is a multi – offset (Fisher *et al*., 1992) attribute analysis technique which involves relating amplitude variations with increasing angle of incidence (or practically, offsets), in order to characterize interfaces and layers (Castagna, 1993; Baker, 1998). Attribute analysis of GPR data allows for extensive exploitation of the information contained in a reflected wavelet, including geometry and detailed material property information. This analysis requires collecting offset dependent reflectivity (ODR) data through common mid-point (CMP) surveys in the field. In the CMP mode, antennas are moved symmetrically about a midpoint increasing the offset, and data collected for the same point on a reflector (assuming a horizontal interface) so that the reflections are recorded for each antenna offset. The antenna offset is subsequently converted to angle of incidence; a plot of reflection amplitudes against the angle of incidence represents the main diagnostic data for AVA analysis (Castagna, 1993, Baker, 1998). The recorded amplitude (A_{obs} (mV)) can be expressed as:

$$A_{obs} = A_{sou} \cdot \frac{C_{TR} \cdot P_{TR} \cdot t}{r} \cdot R \cdot exp^{(-\alpha r)} \tag{1}$$

Where: C_{TR} is antennae coupling with the ground surface; *t* here is defined as transmission loss through any interface in the overburden above the target reflection; P_{TR} is antennae pattern;

A_{sou} *(mV)* is the source amplitude; α *(m^{-1})* is the attenuation coefficient; r (m) is the ray path length. *R* is the absolute reflection coefficient.

The GPR AVA technique has its origin from seismic reflection processing (as with other common processing methods). It assumes isotropic source radiation (and reception) for GPR and also, far – field conditions. GPR antennae radiate EM energy as waves travelling in a hemispherical wave front into the ground and, typically show a strong directionality in radiation and reception with respect to amplitude and/ or frequency of the signal when used for surface surveys. The antennae patterns depend on the properties of the media in which the GPR signal is radiated into: for example, the pattern in air is different from that in water, oil or in rocks; it must, therefore be accounted for in AVA analysis. Antennae (transmitter and receiver) patterns (P_{TR}) are important sources of noise which must be accounted for in AVA analysis.

This paper reports the results of the measurement of composite antenna pattern in the field and comparison with numerically derived patterns. In the context of this paper, antennae patterns refer to the composite of transmitter radiation and receiver sensitivity patterns when placed on the ground surface. Secondly antenna patterns described here relate to only transverse electric (TE) mode GPR data. The field site is Threshfield quarry, Yorkshire, United Kingdom, extracting rocks of Carboniferous Limestone. The next section reviews theoretical solutions proposed in published research for characterizing antennae pattern in a dielectric half space e.g. air – limestone boundary. I then describe measurement of the composite antennae pattern in this field site from numerical modelling and field transillumination surveys. Both numerical and field data were processed using Reflex-Win Version 3.5.1 software (Sandmeier, 1997-2004). Processing comprises: de-wow (for field data), band – pass Butterworth filtering (250-750MHz), geometric spreading and envelope, or Hilbert transform. Finally I assess the appropriateness of the obtained patterns in correcting ODR data for AVA analysis.

Theoretical radiation patterns

Analytical solutions for the radiation pattern of a dipole antenna located on a planar boundary between two semi-infinite media have been presented by several authors e.g. Engheta *et al.,*(1982), describe the far-field radiation pattern of an infinitesimal dipole antenna as having a sharp maximum in the TE plane at the air to ground critical angle (figure 1, black lines).However, GPR surveys are typically at finite distances from the source antenna (i.e. near - field), with penetration depth limited by attenuation. In most applications of GPR, targets are within 2-20λ of the radiation antenna at the dominant signal frequency (Bradford and Deeds, 2006).
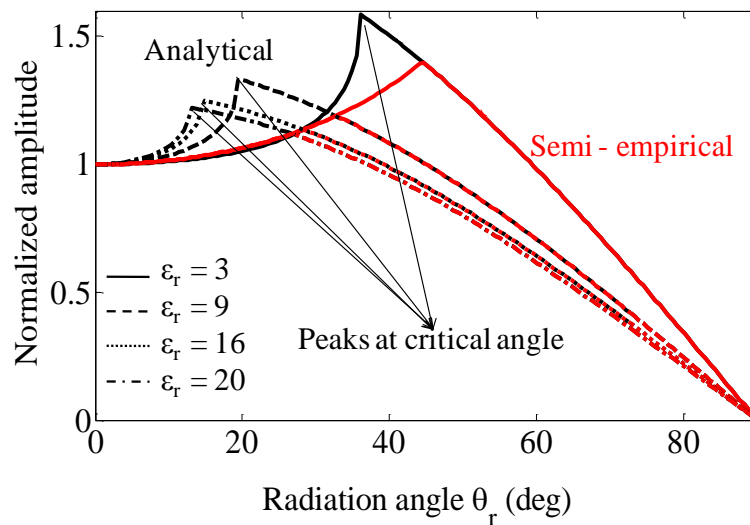
Figure 1. Theoretical radiation patterns as described in Enghetta *et al.,* (1982) and Bradford (1998).

Near-field patterns determined experimentally and through numerical modelling differ from far-field patterns e.g. Annan *et al.,* (1975); Holliger and Bergman (1998); Valle *et al.,*(2001); and Radzevicius *et al.,*(2003). They reported that near – field TE patterns are broader than the far – field patterns and that the peaks, which are predicted to occur at the critical angle in the analytical patterns, are absent. Annan *et al.,* (1975) measured experimentally the antenna radiation pattern in oil at distances of 3 to 6 λ (at the characteristic signal frequency) from the source, and attributed the discrepancy between the far – field and near – field patterns to the fact that their measurements were made at finite distances from the source. In a modelling study, Holliger and Bergman (1998) reported similar deviations from the far – field patterns, and concluded that the discrepancy may reflect generic inadequacies of the asymptotic far-field solutions which, being optical, do not include the effects of interference; rather they show sharp discontinuous peaks at the critical angle. As the distance from source is increased, experimental patterns become more like theoretical patterns (e.g. Annan, 1975) but full convergence is not observed even at a distance of 40 λ in the dielectric (Valle *et al.*, 2001). In agreement with these findings, Bradford and Deeds (2006) suggest constructing case specific antennae patterns that do not depend on the far-field approximation. They also reported that a semi-empirical radiation pattern (figure 1, red lines) derived by Bradford (1998),which they say is similar to laboratory measurements of Annan *et al*., (1975), yielded good results when used to correct offset dependent reflectivity, ODR data in AVA analysis. The semi- empirical pattern has the form sec (θ) at low angles of incidence and converges on the far-field pattern at higher angles of incidence.

In a modelling study, validated by laboratory measurements, Radzevicius *et al.,* (2003), showed that near-field antennae patterns result from interference between lateral and surface waves and therefore depend on electrical properties of the ground and observation distance. Figure 2 shows the different fields generated by a dipole source located on an air-ground interface; the spherical waves *A&C* propagate radially outward into the air and dielectric respectively. Secondary boundary waves *B&D* are also observed and exist to maintain the boundary conditions: continuity of the electric and magnetic flux densities orthogonal to the interface, and continuity of the tangential electric and magnetic fields across the interface. Wave *B,* a

head or lateral wave, propagates into the dielectric with its wave front inclined at the critical angle of the boundary:

$$\theta_{ic} = sin^{-1}\left(\frac{1}{\sqrt{\varepsilon_r}}\right) \qquad (2)$$

ε_r is relative permittivity and θ_{ic} is critical angle.

Wave *B* arises from energy travelling along the boundary, which is continuously refracting at the critical angle. Wave *D* is an evanescent wave coupled to wave *C* and decays rapidly away from the surface. Wave *B* only exists in spatial regions where the position vector (or wave front inclination), makes an angle greater than critical angle of the boundary relative to the vertical axis.

Moving from the vertical (i.e. at normal incidence), the radiation pattern is dominated by the spherical wave (C) but as the angle increases it is determined by the spherical and lateral waves (B & C). In the area of the critical angle, a region of interference between the two waves (B & C) exists, where they cannot be separated, beyond this region, the waves are separable. The 'humps' or maxima observed in near-field antennae patterns are produced by the interference between the spherical and lateral waves (Radzevicius *et al.,* 2003). These patterns depend on the electrical properties of the dielectric and observation distance. Increasing dielectric permittivity and distance from source increases directivity of the antennae; the radiation peaks move towards the critical angle with distance and dielectric permittivity (Radzevicius, *et al.,* 2003).
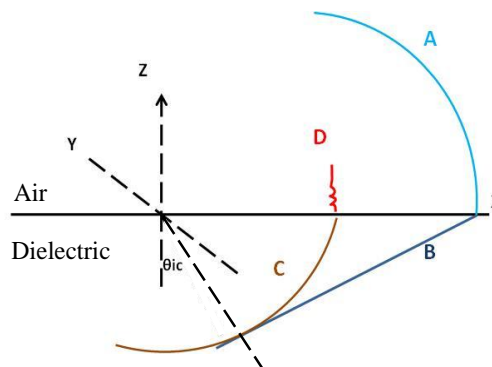

Figure 2. Wave fields about a dipole source on an air – dielectric (earth) interface, modified from Annan (1975). θ_{ic} is critical angle, see text for explanation.

GPR surveys are conducted using two antennae for transmitting and receiving; amplitudes recorded thus contain the composite effect of transmitter (direction in which the energy leaves the antenna) and receiver (direction in which the energy is recorded). In media such as water or oil, the composite antennae pattern can be obtained by moving the receiver around the transmitter to observe field variations (e.g. Annan *et al.,* 1975 and Radzevicius *et al.,* 2003). In solid rock the composite pattern can be observed by measuring the variation in amplitude of the direct wave as a function of propagation direction through a homogeneous material in transillumination surveys (figure 3). This approach is applied here through numerical modelling and field measurements.

In AVA analysis, ODR data are obtained using the CMP survey geometry. The geometric relationship between the different rays, i.e. lateral wave and surface waves, is the same for both

transillumination and CMP geometry, provided the observation distance in transillumination surveys is equivalent to the depth to the shallowest reflection on a CMP section, and provided the direct wave amplitude is sampled at angles equivalent to emergence angles for the target reflection (compare figures 3a and 3c). After correcting amplitudes for propagation effects, composite antennae patterns may be observed by measuring the amplitude variations as a function of the direction in which the energy is radiated and received (e.g. in Jiao *et al*., 2000).The procedure assumes the material is homogeneous and the reflector in the CMP survey is flat.

Measurement of composite antennae pattern

Numerical simulations of antennae pattern

Numerical models were generated from the 3D finite difference time domain (FDTD) code GprMax (Giannopoulos, 2005). FDTD codes have been successfully used to characterize near-field GPR antennae radiation characteristics: Holliger and Bergman, (1998); Radzevicius *et al.,*(2003) and Deparis and Garambois,(2009).The FDTD approach to numerical modelling involves discretizing both space (Δx, Δy,andΔz) and time (Δt) domains so that the model consists of a grid of rectangular, isotropic and homogeneous FDTD cells. The numerical solution in GPR modelling is progressively obtained in the time domain using a discretized form of Maxwell's equations which are applied in each FDTD cell. For each time step, the electromagnetic (EM) field advances in the FDTD grid with an elapsed time Δt so that the number of time steps determines the total time window. Detailed description of the code and examples can be found in Giannopoulos, (2005). The model geometry (figure 3a), consists of a block of limestone of thickness equivalent to the observation distance for which the radiation pattern is found (e.g. bedding fracture reflection in a CMP section).
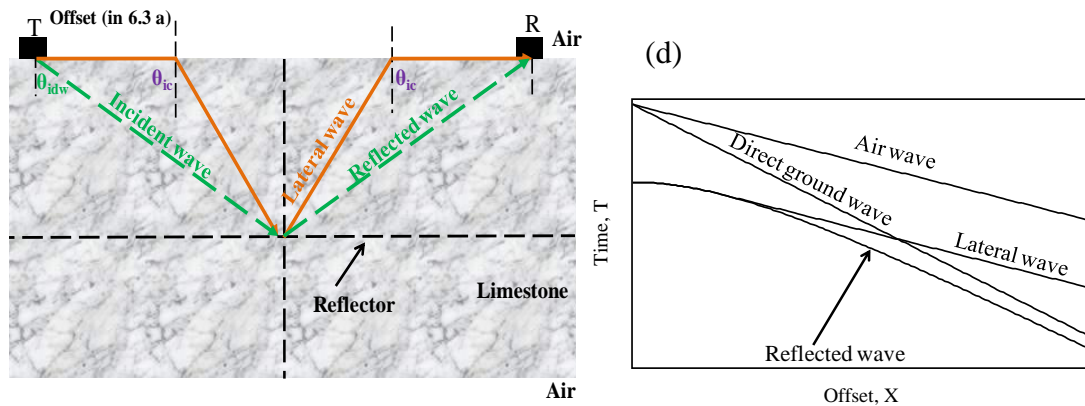
(a)
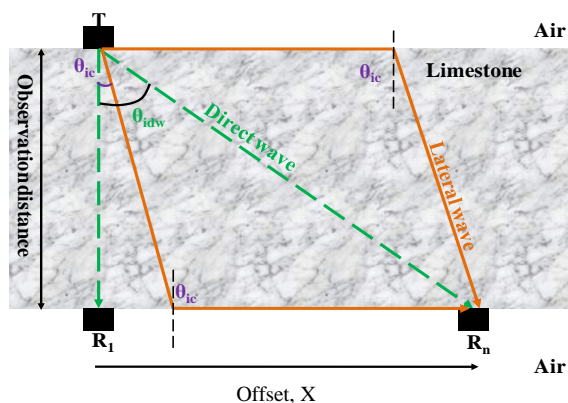
(b)
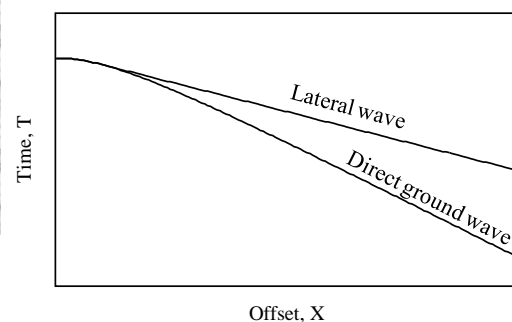
(c)

Figure 3. (a) FDTD transillumination survey geometry and (b) corresponding TX plot showing the direct ground wave and lateral wave ray paths. (c) CMP survey geometry and (c) corresponding TX plot showing the direct wave, reflected wave and lateral wave travel paths.

Antennae are first specified in GprMax on both sides of the block so that the direct wave impinges on the block edge at normal incidence (figure 3a); the receiver is then moved in increments equivalent to the sampling interval of the field CMP thus increasing the radiation angle with each increment. A Hertzian dipole with a 500MHz Ricker source pulse was specified. The discretization step was set to 0.01m ($< \lambda/10$), to reduce numerical dispersion (Giannopoulos, 2005). Figure 4 is a snapshot of FDTD generated field for a Hertzian dipole located on an air – limestone interface after an elapsed time of 5 ns. The waves described in figure 2 are labelled A - D.
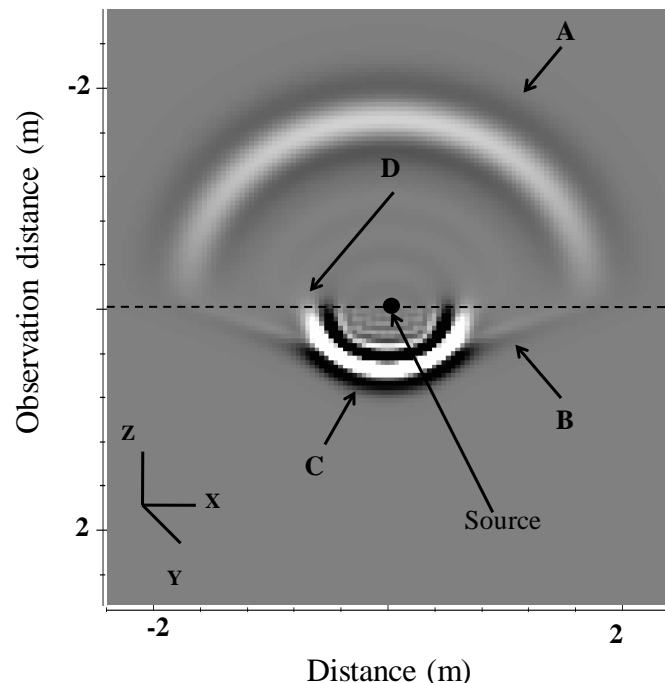

Figure 4.Snapshot of a TE component of the radiated field around a 500MHz hertzian dipole located on an air – limestone interface at a distance of 0.5m from the dipole (2.5λ in limestone). The snapshot was taken after an elapsed time of 5 ns. $\varepsilon_{r \text{ limestone}} = 8$, $\varepsilon_{r \text{ air}} = 1$, $\sigma = 0$ for both limestone and air.
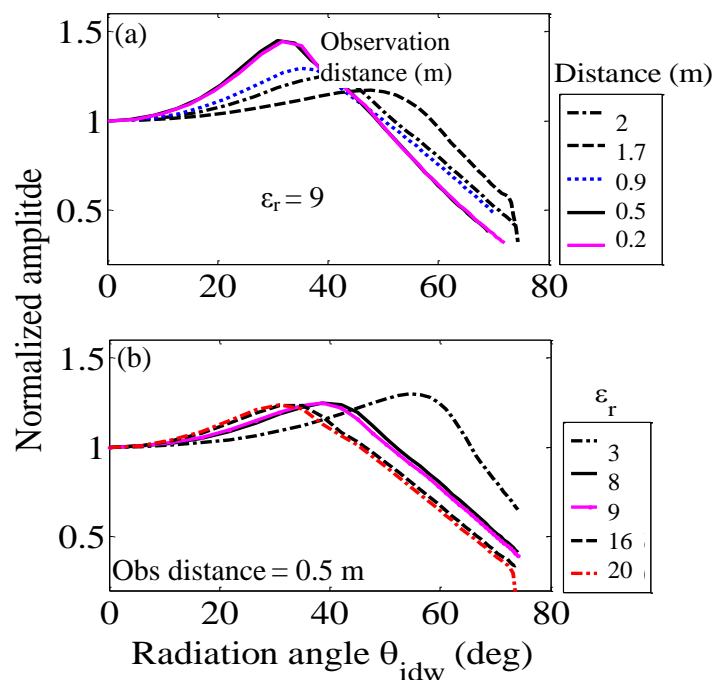
Figure 5. FDTD antenna radiation pattern with (a) observation distance and (b) relative permittivity.

To test the dependence of antennae patterns on observation distance, the latter was varied for a limestone block with $\varepsilon_r = 9$ from: 0.2m to 2.0m (figure 5 a). The dependence on permittivity was tested by varying the ε_r for a 0.5m thick limestone block from: 3 to 20 (figure 5 b). The figure shows only the radiation pattern, which is the square root of the composite antennae patterns measured. By the principle of reciprocity, antennae patterns are the same whether used for transmitting or receiving (White, 1965; Kähler and Meissner, 1983). Electrical conductivity was not included (i.e. set to zero in GprMax) as it has been shown (Radzevicius *et al.,* 2003) not to affect the shape of the antennae patterns.

Modelled antennae pattern shapes, and dependence on both relative permittivity and observation distance found here, agree qualitatively with previous findings: Annan *et al.,*(1975) and others. The characteristic 'hump' in the critical angle region is seen and it becomes narrower with increasing relative permittivity and decreasing observation distance. These findings suggest that antennae patterns can be estimated practically, through transillumination surveys in the field which, if successful, will give site - specific and hence appropriate antennae patterns necessary to correct ODR data in AVA analysis. Field measurement of antennae patterns is discussed in the following sections. For comparison, numerical radargrams will be shown in the next section.

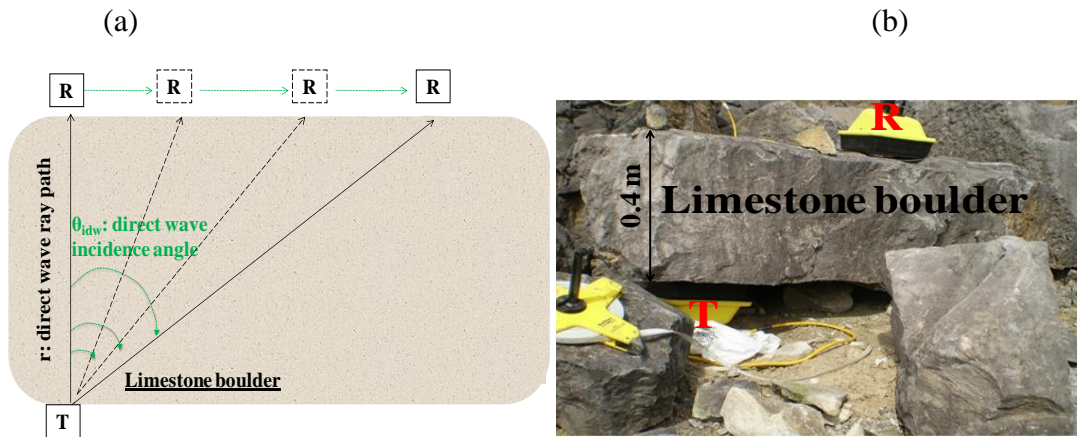Field transillumination surveys to measure antennae patterns

Figure 6 (a) Boulder transillumination survey geometry; (b) a picture of a 0.4 m thick boulder with antennae placed on top and bottom surfaces of the boulder.

The 500MHz GPR system was used to collect TE mode direct wave amplitude data as a function of direction through a transillumination survey across limestone blocks with thicknesses corresponding to the observation distance in the numerical models (figure 5 a). Figure 6a shows the survey geometry and table 1 summarizes acquisition parameters.

Table 1.Boulder transillumination (antennae patterns) data acquisition parameters.

Parameter	Value
Survey type/Antennae polarity	Transillumination /TE
Sampling interval (ns)	0.05
Trace increment (m)	0.02
Recording window / record length (ns)	200
Stack	64
Frequency (MHz)	500

The idea was to measure the composite effect of the antenna radiation and receiver sensitivity patterns, necessary in order to ascertain how close the numerical approximation is to *in - situ* field conditions and vice versa. Processing applied to the data includes: de-wow, a 250 – 750 MHz band – pass Butterworth filter and geometric spreading correction which was applied by multiplying each amplitude, recorded for a particular offset, by the ray path length (r in figure 6), which is the same as the observation distance. Because limestone is very resistive, and surveys were done on dry limestone boulders, only spreading attenuation was considered. The amplitude used is the local maximum of the envelope function over a time window equivalent

to the duration of the GPR wavelet. Some numerical data are shown alongside their field equivalents, in figures 7 (a - d), 9 (a - d) and 11 (a - d). Processed field and numerical radargrams are compared in (a) and (b); ray paths for the waves are shown schematically in (c), and corresponding amplitudes in each of these as a function of incidence angle (direct wave direction) are shown in (d). Amplitudes are normalized relative to the average of the most stable region i.e. noise free region in each case; this was done in order to allow a comparison of the shapes of the patterns obtained using both field and numerical approaches.
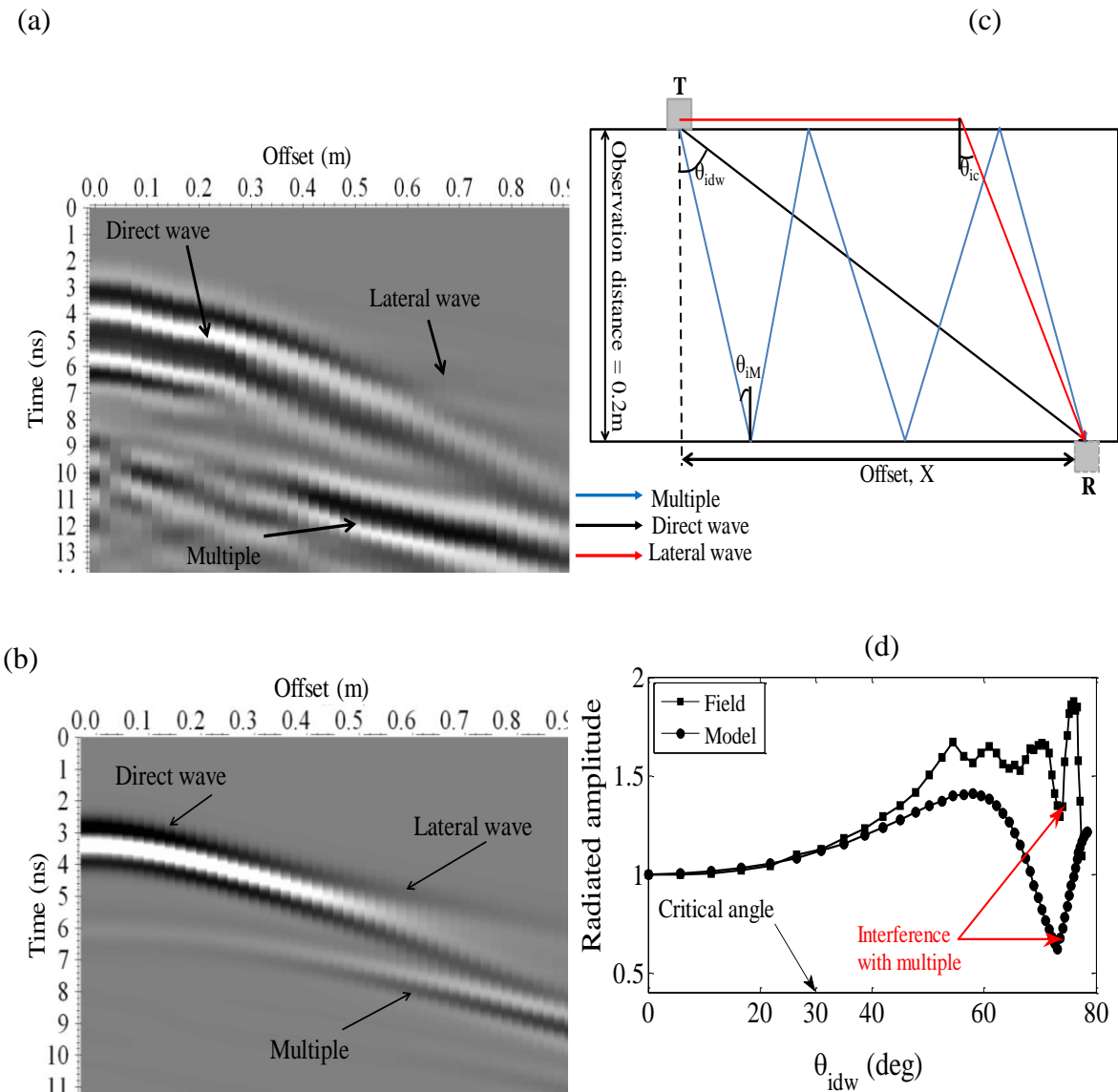

Figure 7 (a) Field and (b) numerical radargrams for a 0.2m thick boulder; (c) shows direct wave, lateral wave and multiple reflection ray paths; and (d) the resulting atennae patterns. θ_{ic} is critical angle, θ_{idw} is direct wave radiation angle and θ_{iM} is incidence angle for the multiple reflection.

Figure 7 shows field and numerical data for a 0.2m thick limestone boulder; both direct wave and lateral waves are distinct beyond the interference region (i.e. $\theta_{idw} > 30°$).
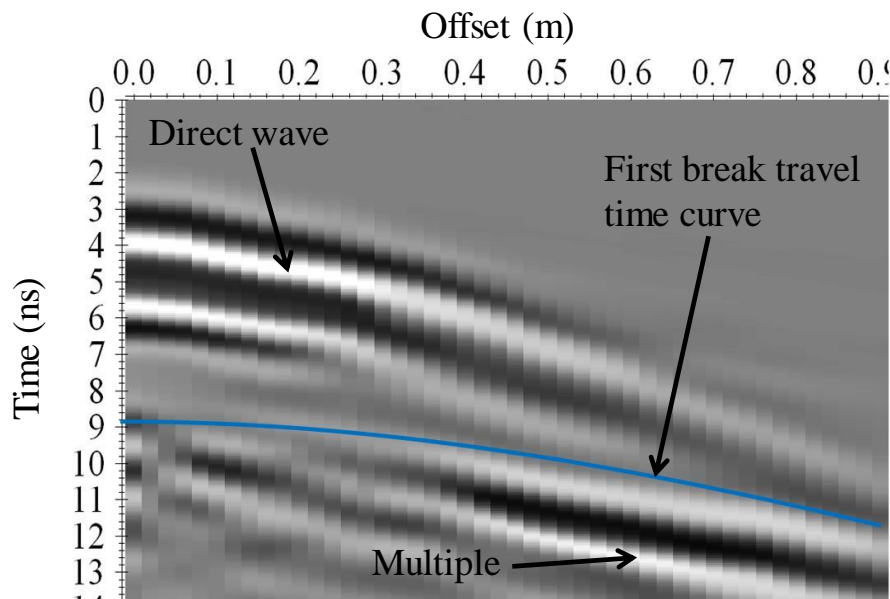

Figure 8. First break travel times for the multiple reflection interfering with the direct wave at high offsets (blue line).

Also seen is a multiple reflection in both numerical and field radargrams, which interferes with the direct wave at high offsets to cause the increase in amplitude observed at high angles (figure 7d). The travel paths for these waves are shown in figure 7c; first break travel times for the direct wave and multiple reflection computed using the geometry in figure 7c are shown in the field radargram in figure 8. the basic shape of field and numerical antennae pattern is similar.

Figure 9 shows antennae pattern data for a 0.4m thick boulder; in addition to the direct wave, the lateral wave is present in both field and numerical radargrams (figures 9a and 9b respectively); these two waves become distinct beyond the critical angle region (i.e. 30°).
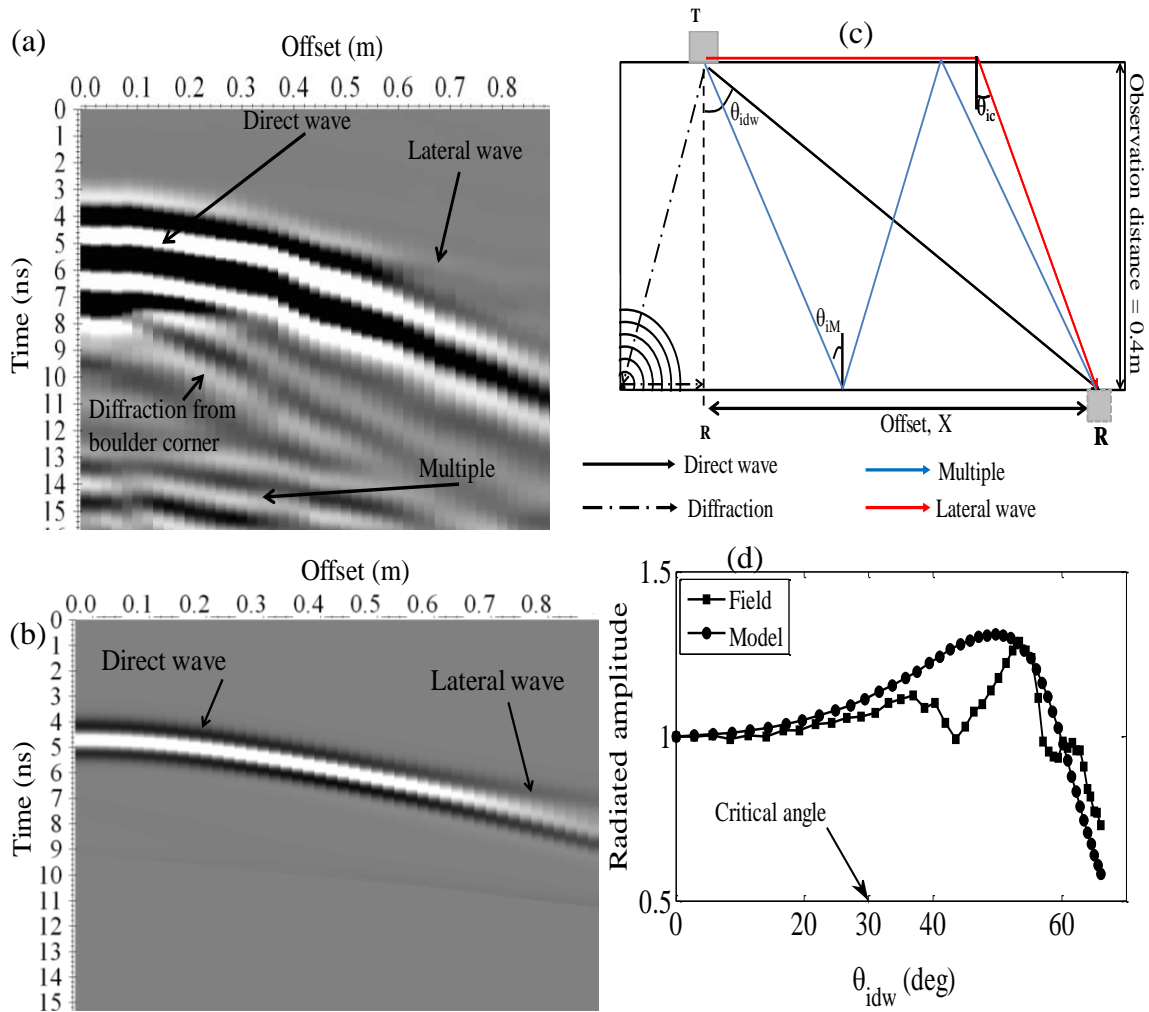
Figure 9 (a) Field and (b) numerical radargram for a 0.4 m thick boulder, (c) shows direct wave, lateral wave, diffracted wave and multiple wave ray paths and (d) the resulting atennae patterns, θ_{ic} is critical angle

An event which appears to interfere with the direct wave at normal incidence is also seen; I have interpreted this event as a diffraction from the boulder corner (figure 9c). At about 12ns, a second event is seen which I have interpreted as a multiple reflection from the two horizontal surfaces of the boulder. To support these interpretations, I computed first break travel times based on the geometry in figure 9c for the two events. These are shown in figure 10; the first break times coincide roughly with these events. While the basic shape of both field and numerical antennae patterns is similar, the diffraction, modifies the field pattern.
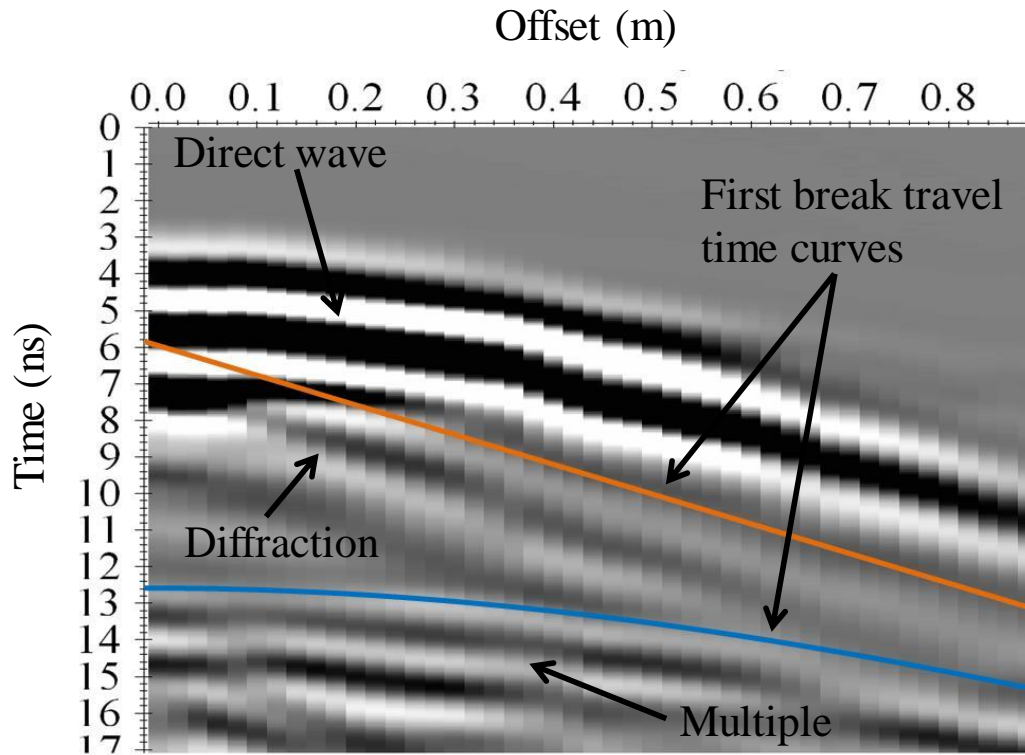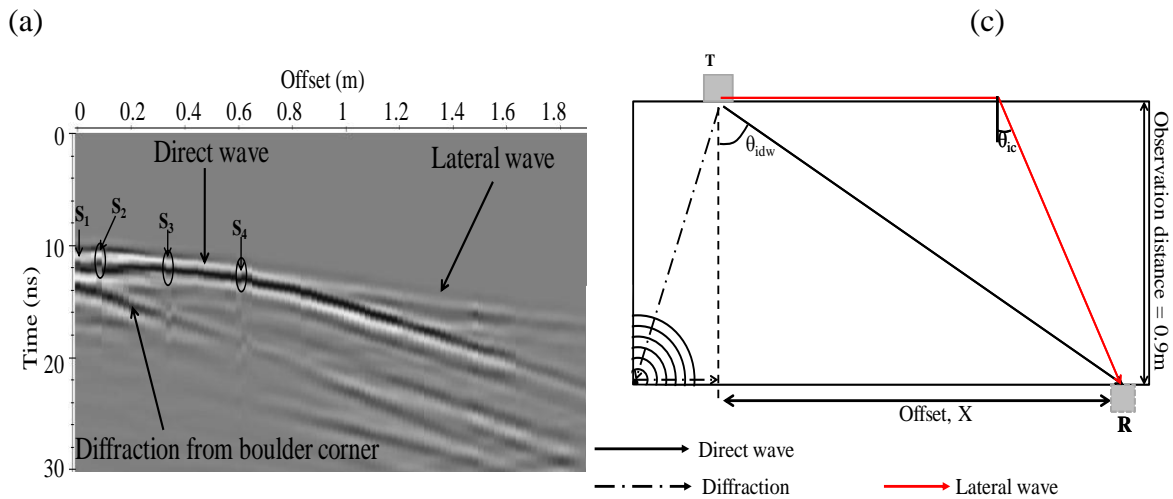
Figure 10. First break travel times for the diffracted wave from the boulder corner (orange line), and the multiple reflection (blue line) in the 0.4m thick boulder in figure 9a.

(a)   (c)
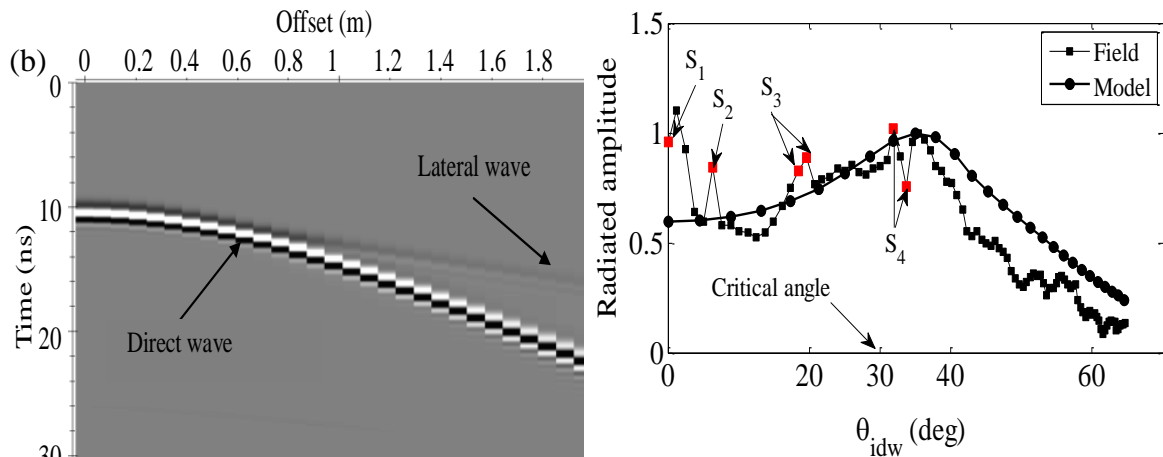

(d)

Figure 11. (a) Field and (b) numerical radargram for a 0.9 m thick boulder, (c) shows direct wave, lateral wave and diffracted wave ray paths and (d) plots the resulting atennae patterns, θ_{idw} is direct wave radiation angle.

As in the 0.2m and 0.4m thick boulders, both numerical and field radargrams for a 0.9m thick boulder (figures 11a and 11b) show the direct ground wave and the lateral wave which interfere in the region of the critical angle (30°), to produce the antennae patternss. In the field radargram (figure 11a), there is an event with the same origin as the direct wave, but diffracting from the boulder corner. At small offsets, it interferes with the direct wave leading to the high amplitudes observed between 0° and 10° (figure 11d). Figure 12 is the field radrgram in figure 11a; first break travel times computed using the geometry in figure 11c for the boulder corner diffraction, coincides with the event.
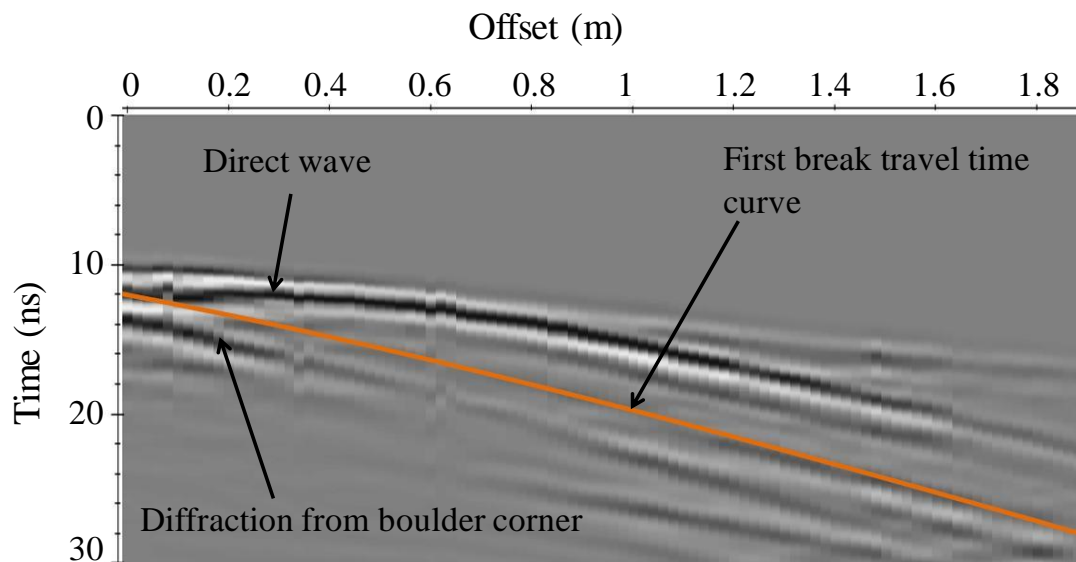

Figure 12 (a) First break travel times for the diffracted wave from the boulder corner (orange line), and the multiple reflection (blue line) in the 0.4m thick boulder in figure 9a.

The 'zig – zag' pattern observed in the field data (figure 11d) between 0° and 6°; 18° and 19°; and between 31° and 33° are due to bad traces (labelled S_1 to S_4 in figure 11d) recorded during

data acquisition (e.g. due to variable coupling with the horizontal boulder surface). Field and numerical antennae pattern shape is broadly similar (figure 11d).

In all examples, the basic shape of the composite antennae patterns is similar and the 'hump' is observed in the region of interference. There is however, some interference in the field data especially at the extremities of the survey offsets (angles). The edges of the boulders along which field data were collected are close enough to the antennae to influence recorded data. To avoid processing interference related artefacts in the field data, antennae patterns, appropriate for each CMP section were modelled numerically using the same approach outlined in this section.

Due interference recorded, can't use the field pattern, rather, will demonstrate with numerical patterns.

Antennae pattern correction applied to CMP data acquired on the quarry floor.
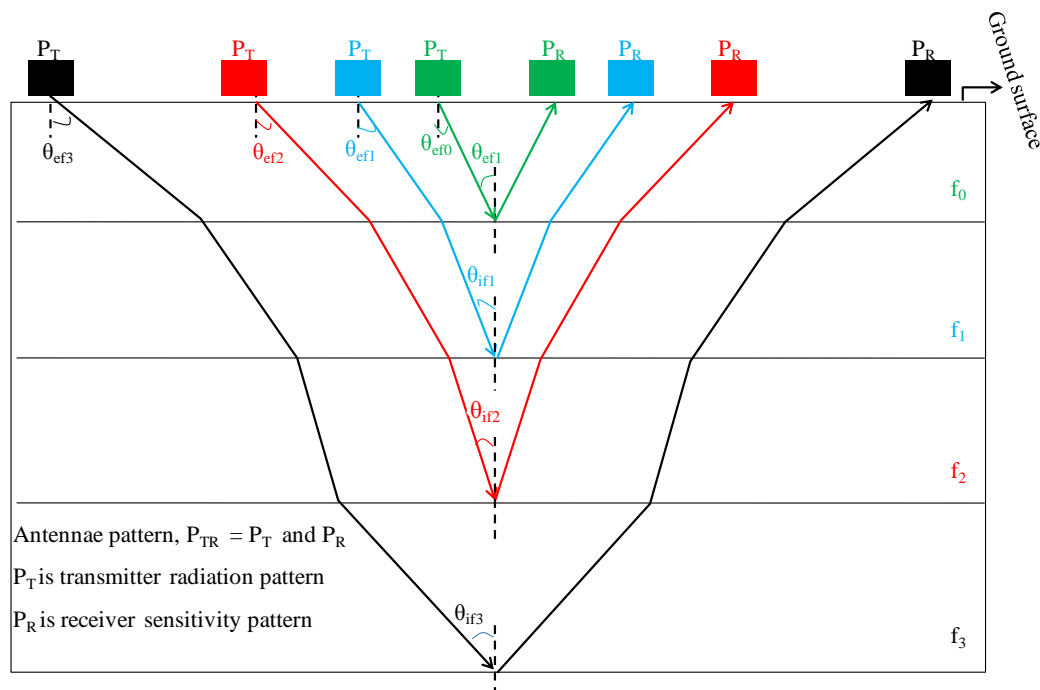

Figure 13. A schematic representation of a CMP geometry showing emergence and incidence angles (i.e. θ_e and θ_i respectively) for successive reflections.

Antennae patterns depend on radiation or emergence angle. Using the CMP survey geometry, each successive wavelet reflected has a different ray path and therefore a different radiation angle i.e. emergence angle for each reflection is different (figure 13). The emergence angle for a ray incident on a horizontal and planar surface is the angle measured from the normal to the surface (figure 13). Antennae patterns for each reflection, for a given CMP offset, need to be evaluated at its emergence angle. The emergence angle is computed iteratively by 1D ray tracing according to Snell's law, assuming horizontal layers with constant thicknesses, and taking account of 1D velocity variations.

CMP data acquisition - CMP data were acquired on the horizontal quarry floor using a PulseEkko Pro GPR system with 500MHz antennas. Antenna offsets ranged from 0.29m to

19m at increments of 0.04m. CMP data were processed using Reflex-Win Version 3.5.1 software (Sandmeier, 1997-2004). To preserve amplitude characteristics which are of interest, minimal processing was applied to the data; de-wow, 250-750MHz band pass Butterworth filter and time zero corrections. The processed data show the presence of 2 reflections labelled f_0 and f_1 (figure 14).

Composite antennae pattern for f_0 was modelled using the numerical approach outlined in section 3.2; evaluated at corresponding emergence angles. The observation distance in each case is the depth to f_0 in the CMP. This is because the antennae patterns are as a result of interference between the lateral wave, which travels on the ground surface (figure 3) and the incident/reflected wave travelling in the ground. Therefore radiation pattern effects are observed at the first interval in a CMP section

Figure 15 shows the process of extracting AVA curve from the reflection: f_0 in the CMP data, 15a shows the raw AVA curve and corresponding numerically derived composite antennae pattern, while figure 15b shows the AVA data corrected for geometric spreading, intrinsic attenuation and composite antennae patterns.
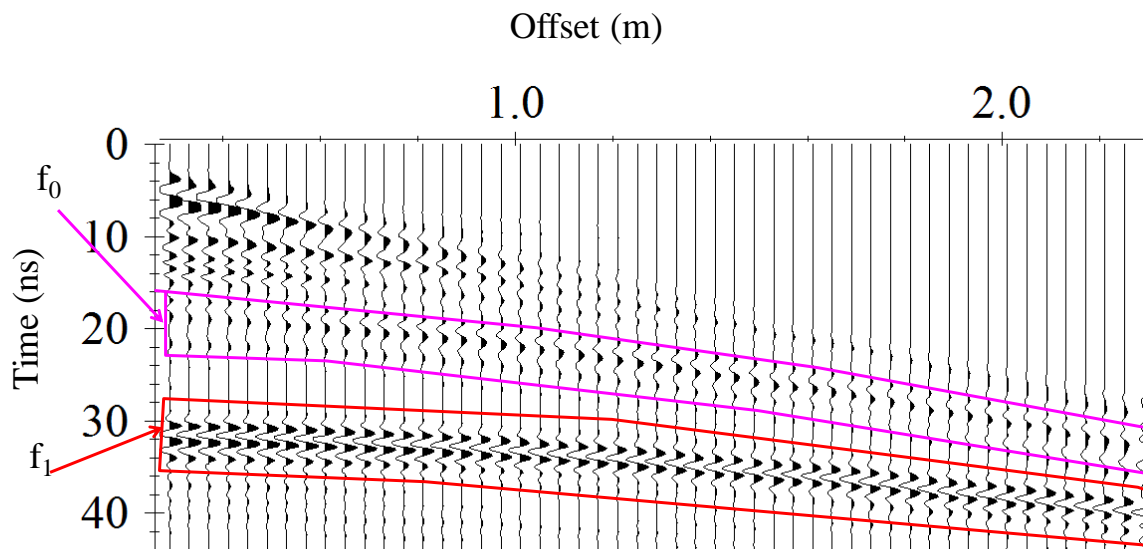

Figure 14. CMP data acquired on the quarry floor showing two reflections: f_0 and f_1.

In the figures, the raw AVA curve shows the effect of antennae pattern; the characteristic 'hump' is seen in both the AVA curve and the antennae pattern. The shape of the AVA curve changes after geometric spreading, conductive attenuation and antennae pattern corrections; the antennae pattern hump is reduced, and amplitudes increase with incidence angle. The AVA curve is qualitatively consistent with its theoretical equivalent, computed using permittivities of the gravel layer and the underlying limestone (i.e. ε_r = 11.9 and 6.3 respectively derived from semblance analysis of the CMP data). Both curves predict increasing amplitudes with incidence angle.
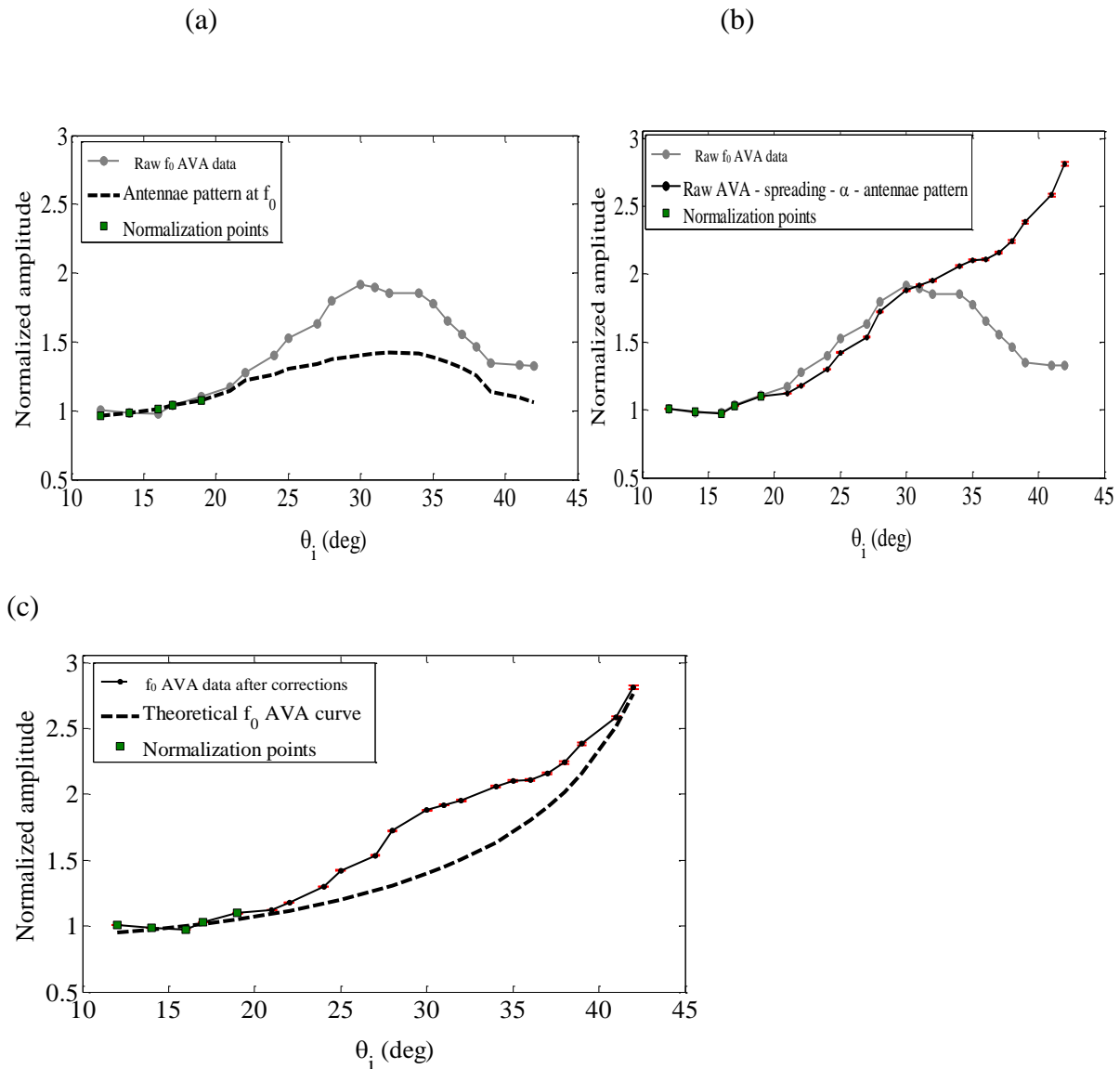
(a) (b)

(c)

Figure 15. (a) Raw AVA and numerically derived antennae pattern for f_0 in the CMP data; (b) f_0 AVA curve after: geometric spreading; conductive attenuation; and antennae pattern corrections. In figure 15c: theoretical AVA for f_0 in the CMP section is shown with the corrected f_0 AVA curve.

DISCUSSION

Antennae patterns include effects of the interference of *lateral* and *body* waves, and this interference, can be measured in the field through transillumination surveys. GPR antennae *radiation patterns* have been characterized using analytical (Engheta, 1982) and semi empirical solutions (Bradford, 1998); through numerical modelling (Annan *et al.,* 1975; Deparis and Garambois, 2009) and laboratory experiments (Annan *et al.*, 1975; Radzevicius *et al.*, 2003). In Deparis and Garambois (2009), antennae patterns were determined numerically. In section 3, I demonstrated the need to estimate case specific antennae patterns in correcting ODR data for AVA analysis and further proposed a means of characterizing the composite antennae

patterns in the field and through numerical simulations. There isn't to the best of the author's knowledge, any existing literature in which *composite antennae patterns* are characterized in the manner applied here, i.e. numerical simulations and field transillumination surveys.

Field transillumination and numerical antennae pattern examples agree broadly; unfortunately due to interference, the field transillumination data could not be used in the example, to correct AVA data for antennae effects. The interference was mostly as a result of measurements made close to rock boulder edges so that the continuously refracting air wave along the boulder edges was interfering with the direct ground wave. Running transillumination surveys as 'far' as possible from boulder edges can lead to better field data and hence *in - situ* characterization of antennae patterns.

In the CMP example presented, antenna pattern for the target reflection was modelled using the numerical approach outlined previously, this was used to correct the raw AVA curve.

CONCLUSION

The preceding analysis demonstrates that *in – situ* measurement of composite antennae patterns in the field can be done through transillumination surveys. Although it was not possible to use the field derived patterns to correct the ODR data, the numerical equivalent yielded satisfactory results, suggesting that carefully conducting the transillumination surveys (i.e. far away from the boulder edges to reduce interference from the airwave) can yield satisfactory results.

REFERENCES

Annan, A. P.,Waller, W. M., Strangeway, D. W., Rossiter, J. R., Redman, J. D. and Watts R. D. (1975). The Electromagnetic response of a low - loss 2 - layer dielectric earth for a horizontal dipole excitation. *Geophysics,* **40**, 285 - 298.

Baker, G. S. (1998). Applying AVO analysis to GPR data. *Geophysical Research Letters*, **25**, 397- 400.

Bradford, J. H. and Deeds, J. D. (2006). Ground-penetrating radar theory and application of thin-bed offset dependent reflectivity. *Geophysics* **71**, K147 - K157.

Bradford, J. H. (1998). Characterizing shallow aquifers with wave- propagation based geophysical techniques: Imaging and attribute analysis. Ph.D thesis, Rice University, United States of America.

Castagna, J. P. (1993). AVO analysis – Tutorial and review in: Castagna J. P and Backus M. M ed. Offset Dependent Reflectivity – Theory and Practice of AVO analysis. Society of Exploration Geophysicists, USA, pp 3 - 36.

Deparis, J. and Garambois, S. (2009). On the use of dispersive APVO GPR curves for thin-bed properties estimation: Theory and application to fracture characterization. *Geophysics*, **74**, J1 - J12.

Engheta. N., Papas, C. and Elachi, C. (1982). Radiation patterns of interfacial dipole antennas. *Radio Science,* **17**, 1157 - 1566.

Fisher, E., McMechan, G. A. and Annan, A. P. (1992). Acquisition and processing of wide-aperture ground-penetrating radar data. *Geophysics*, **57**, 495 - 504.

Giannopoulos, A. (2005). GprMax2D/3D Version 2.0 User's manual.

Holliger, K. and Bergman, T. (1998). Accurate and efficient FDTD modelling of ground - penetrating radar anttena radiation pattern. *Geophysical Research Letters*, **25**, 3883 - 3886.

Inan, S. U. and Inan, S. A. (2000). Electromagnetic waves. Prentice – Hall, Inc, Upper Saddle River, USA.

Jiao, Y., McMechan, G. A., and Pattinelli, E. (2000). In situ 2 - D and 3 - D measuremnts of radiation patterns of half - wave dipole GPR antennas. *Journal of Applied Geophysics*, **43**, 69 - 89.

Kähler, S. and Meissner, R. (1983). Radiation and receiver patterns of shear and compressional waves as a function of Poisson's ratio. *Geophysical Prospecting*, **31**, 421 - 435.

Radzevicius, S. J., Chen, C., Peters, Jr. L. and Daniels, J. J. (2003). Near-field dipole radiation dynamics through FDTD modelling. *Journal of Applied Geophysics,* **52**, 75 - 91.

Valle, S., Zanzi, L., Sgheiz, M., Lenzi, G. and Friborg, J. (2001). Ground Penetrating Radar Antennas: Theoretical and Experimental Directivity Functions. *IEE Transactions on Geoscience and Remote Sensing,* **39**, 749 - 758.

White, J. E. (1965). Seismic waves: Radiation, Transmission and Attenuation. Vol. 1. McGraw - Hill, New York.